Progress Towards a One-Electron Model for the Non-valence Correlation-bound Anions of Polycyclic Aromatic Hydrocarbons

Abstract. A one-electron model Hamiltonian is used to characterize the non-valence correlation-bound (NVCB) anions of hexagonal polycyclic aromatic hydrocarbons (PAHs) $C_{6n^2}H_{6n}$ ($n = 3-7$). The model incorporates atomic electrostatic moments up to the quadrupole, coupled inducible charges and dipoles, and atom-centered repulsive Gaussians to describe the interaction between the excess electron and PAH. These model components are parameterized on and validated against all-electron calculations. Good agreement is found between the static dipole polarizabilities obtained from the model and those from PBE0 density functional theory and second-order Møller-Plesset perturbation theory calculations. In the model, charge flow dominates the in-plane polarizability of PAHs larger than $C_{54}H_{18}$, yielding an approximately quadratic scaling of the mean polarizabilty with the number of carbon atoms. Inclusion of electrostatic interactions decreases the EBEs for the largest PAHs considered by about 20% and shift charge distribution from above and below the plane of the ring system toward the periphery. Analysis of the electrostatic and polarization interactions provides insight into qualitative trends in the electron binding energy and the charge distribution of the lowest energy NVCB anion.

Keywords: Non-valence correlation-bound anion, Polycyclic aromatic hydrocarbon, Model Hamiltonian, Weak-interaction, Polarizability

1. Introduction

Bound anions of molecules and molecular clusters can be divided into two main categories, valence and non-valence [1, 2]. Valence anions result from electron capture into energetically low-lying valence orbitals with the excess electron being localized near the molecular frame. Non-valence anions represent a distinctly different class where the excess electron is captured into a diffuse orbital with long-range interactions dominating the binding [1, 3–7]. In general, both electrostatics and long-range dispersion-like correlation can be important, but one of these may dominate over the other depending on the system. The two limiting cases are referred to as non-valence electrostatically-bound (NVEB) [8–11] and non-valence correlation-bound (NVCB) anions. There is growing body of experimental and theoretical studies of NVCB anions including fullerenes (e.g., C_{60} and C_{240}) and their clusters $(C_{60})_n$ [12–15], certain water clusters [10, 15–22], $(NaCl)_n$ clusters [23], Xe_n clusters [24], C_6F_6 [6, 25, 26] and $(C_6F_6)_n$ clusters [27, 28], and polycyclic aromatic hydrocarbons (PAHs) [29].

The application of ab initio methods to NVCB anions presents a challenge because both an accurate treatment of electron correlation and the use of flexible basis sets are crucial. The correlation effects responsible for stabilizing NVCB anions are different from near degeneracy effects that arise from small HOMO-LUMO gaps. When starting from a Hartree-Fock (HF) [30–32] reference in treating an NVCB anion, it is essential to include configurations that allow the orbital occupied by the excess electron to, "relax," in response to dispersion-type correlation associated with configurations where the excess electron and a valence electron are both excited [10]. By definition, NVCB anions are unbound in the HF approximation, and with the use of flexible basis sets containing diffuse functions, the excess electron occupies a discretized continuum (DC) orbital in the HF wavefunction. Methods that account for electron correlation, including second-order Møller-Plesset perturbation theory (MP2) [33] and coupled cluster with single, double, and perturbative triple excitations (CCSD(T)) [34], fail to recover the bound anion when starting from a HF reference wavefunction that has collapsed onto a DC level [10, 16].

Density functional theory (DFT) methods based on the local density approximation (LDA) or the generalized gradient approximation (GGA) will fail to accurately describe NVCB states. The exchange-correlation density functional in such methods cannot describe the asymptotic, non-local electron correlation that stabilizes NVCB anions [35]. However, DFT functionals employing a non-local correlation potential show promise. Recently, it was shown that the van der Waals density functional rev-vdW-DF2 [36] improves upon semi-local functionals in describing the image potential states (IPSs) of graphite, graphene, and carbon nanotubes [37]. IPSs are unoccupied states lying between the Fermi level and the vacuum level of a solid, in which an excess electron can be trapped by an attractive long-range self-induced image potential. The underlying physics stabilizing IPSs, long-range electron correlation effects, is fundamentally the same as that leading to NVCB anions.

Electron affinity equation-of-motion coupled cluster with single and double excitations (EA-EOM-CCSD) [38] and electron affinity equation-of-motion MP2 (EA-EOM-MP2) [39, 40], have been used frequently in past studies of NVCB anions [3, 10, 16, 23, 29]. These methods are capable of accurately describing NVCB anions, but they are computationally demanding, $O(\mathcal{N}^6)$ for canonical EA-EOM-CCSD and $O(\mathcal{N}^5)$ for canonical EA-EOM-MP2, where $\mathcal{N}$ is size of the orbital basis. There have been efforts made towards lowering the scaling of EOM-CCSD calculations. In particular, a nearly linear scaling version employing domain-based localized pair natural orbitals (DLPNO) has been introduced for evaluating ionization potentials and a quadratic scaling approach had been developed for electron affinities [41, 42]. However, the approximations that enable the low scaling can introduce errors on the order of tens to a hundred meV. While these are tolerable for ionization potentials, they are not acceptable for NVCB anions where binding energies are typically of the same order as these errors. The steep computational scaling of conventional EOM methods render them unsuitable for characterizing the NVCB anions of systems with hundreds to thousands of atoms.

An alternative approach to treating NVCB anions involves the use of a one-electron model Hamiltonian. The diffuse nature of non-valence anions allows one to make approximations in treating the interactions between the excess electron and the electrons of the molecule or cluster. These interactions involve electrostatics, dispersion, polarization, and exchange. The corresponding potentials in the model Hamiltonian are parameterized using the results of all-electron quantum mechanical (QM) calculations. The dispersion-like correlation effects present in a many-electron treatment can be recovered in a one-electron model upon integration of the excess electron's degrees of freedom over a model polarization potential [43]. The long-range electrostatic potential of the molecule can be described by atom-centered point multipoles. In past work electron exchange, charge penetration, and orthogonality have been accounted for via model potentials, similar in spirit to the pseudopotentials which are used to approximate core electrons in electronic structure calculations [18–21]. One-electron model Hamiltonians have been used to study the NVCB anions of spherical fullerenes and fullerene clusters composed of tens to hundreds of atoms [13–15] Additionally, such models have been applied in theoretical studies of a solvated electron [19–21, 44] and water cluster anions [15, 17, 18]. An inherent advantage of model approaches over all-electron ab-initio treatments, is the ability switch parts of the potential on and off. This affords insight into the magnitude and nature of different contributions to the binding of an excess electron.

This work studies the NVCB anions of hexagonal PAHs in the series $C_{6n^2}H_{6n}$, $n = 3 - 7$, using a one-electron model Hamiltonian implemented in the code PISCES [45]. These hexagonal PAHs consist of a planar set of fused six member rings formed by an sp^2 hybridized network of carbon atoms. In a distributed multipole analysis, the edge carbon and hydrogen atoms have sizable atomic charges and dipoles due to the electronegativity difference of the atoms. However, the molecules are neutral and have no net dipole by symmetry, so the leading order molecular electrostatic

moment is the quadrupole, Θ^{mol}, moment. The only independent component of Θ^{mol} in a traceless Cartesian representation is that which is normal to the molecular plane $\Theta^{\mathrm{mol}}_{\mathrm{zz}}$, as $\Theta^{\mathrm{mol}}_{\mathrm{xx}}=\Theta^{\mathrm{mol}}_{\mathrm{yy}}=-\frac{1}{2}\Theta^{\mathrm{mol}}_{\mathrm{zz}}$. When described in terms of atomic multipoles, $\Theta^{\mathrm{mol}}_{\mathrm{zz}}$ has contributions from atomic quadrupoles Θ_{zz} largely associated with the carbon atoms as well as charges and dipoles arising from the edge C-H bonds [46]. In a study employing EA-EOM-MP2, it was shown by Voora and Jordan that the charge density of the natural orbital occupied by the excess electron is somewhat localized around the periphery of PAHs such as hexabenzocoronene ($C_{42}H_{18}$) [29]. The authors attributed this to an attractive electrostatic interaction between the excess electron and the positively charged hydrogen atoms.

The work of Voora and Jordan [29] was motivated in part by an experimental study performed by Craes et al. on the IPSs of nanostructures called graphene quantum dots (GQDs). GQDs are closely related to PAHs [47], as they can be made in a variety of shapes, sizes, and the edge carbon atoms can be terminated by hydrogen depending on the synthetic approach [48]. Using scanning tunneling microscopy, Craes et al. mapped the spatial modulation of the local density of states corresponding to the first IPS of a hexagonal GQD with an area of 11 nm^2. The LDOS was dominated by a contribution with strong intensity at the center of the GQD and vanishing intensity at the edges. This contrasts the NVCB anions observed by Voora and Jordan, where the excess electron's charge distribution localized near the edge C-H bonds of PAHs. One might expect that for sufficiently large PAHs with appreciable metallic character, the polarization potential stabilizing their NVCB anions would approach that which binds IPSs on GQDs producing a charge distribution that resembles the LDOS maps of Craes et al. However, the GQDs synthesized by Craes et al. were larger than the PAHs considered by Voora and Jordan, were likely terminated by unsaturated carbon atoms [49] rather than hydrogen atoms, and there was an Ir(111) substrate supporting the nanoflakes. To the best of our knowledge there are no papers that perform a similar analysis on hydrogen-terminated GQDs. These factors make it difficult to compare theoretical results on gas phase NVCB anions to the experimental studies on IPSs of GQDs. A related question is whether or not the edge localization Voora and Jordan observed persists in the NVCB anions of PAHs larger than $C_{42}H_{18}$. Whether or not the edge localization is purely an electrostatic effect is an open question as well. Here we investigate these phenomena further using a one-electron model Hamiltonian.

The polarization potential in a model Hamiltonian treatment constitutes the crucial component, as it effectively accounts for the electron correlation responsible for stabilizing NVCB anions [43]. This work makes use of Mayer and Åstrand's model, which includes both atomic anisotropic dipole polarizabilties and fluctuating charges [50, 51]. The charge fluctuation method in the Mayer-Åstrand model is similar to that of Rappé and Goddard [52], which has been scrutinized due to its tendency to exaggerate polarization in insulating systems and unphysical behavior when molecular geometries deviate from equilibrium structures [53–55]. The latter point is not an issue here as molecular geometries are taken to be rigid, but the

former is worth considering. The accuracy of the model is assessed via comparison to polarization potentials and static dipole polarizabilities from all-electron calculations. Further analysis is performed by decomposing the model polarizabilities and polarization potentials into contributions from inducible dipoles and charge flow. Some QM methods struggle to accurately predict dipole polarizabilities in highly conjugated systems. An overshoot in dipole polarizabilities has been reported for conjugated molecular chains [56], 1D and 2D acenes, and 1D, 2D, and 3D H_2 clusters [57], as described by LDA and GGA density functionals. With this in mind, we calculate and compare reference dipole polarizabilities from HF [30–32], MP2 [33], Coulomb-attenuating B3LYP (CAM-B3LYP), [58] and PBE0 [59]. While CAM-B3LYP and PBE0 are based upon GGAs, both include some fraction of exact HF exchange making them less prone to excess delocalization when compared to pure GGAs. CAM-B3LYP includes different fractions of exact exchange at short-range and long-range with an error function smoothly connecting the two regions.

This article serves as an in-depth study of the nature of the lowest energy NVCB anions of hexagonal PAHs and a report on our progress in developing a one-electron model Hamiltonian to describe them. In section 2.1, the one-electron model Hamiltonian is detailed. Section 2.2 describes the potential terms in the model Hamiltonian. Section 2.3 explains how the model potential is parameterized and the process for obtaining reference polarization potentials, static dipole polarizabilities, and electron binding energies (EBEs). Section 3.1 makes comparisons between the model and reference polarizabilities for $C_{6n^2}H_{6n}$, where $n = 1 - 7$, and provides an analysis of the charge flow and inducible dipole contributions to the in-plane and out-of-plane dipole polarizabilities. A similar analysis is performed in section 3.2 for the polarization potentials. In section 3.3 the quality of the of the full model potential is assessed via comparison to EA-EOM-MP2 and EA-EOM-CCSD results for coronene ($n = 2$). Then, trends in EBE are reported in section 3.4 for the lowest energy NVCB anion of PAHs $n = 3 - 7$. In section 3.5 the full model potential is dissected into contributions from electrostatics, polarization, and repulsion providing insight into the impact of electrostatic effects. Additionally, density differences are reported in section 3.5 to illustrate the effect electrostatics has on the excess electron's charge distribution in these NVCB states.

2. Methods

2.1. One-electron Model

The model Hamiltonian employed in this work for an excess electron interacting with a PAH is:

$$\hat{H}(\boldsymbol{r}) = \hat{T}(\boldsymbol{r}) + \hat{V}_{es}(\boldsymbol{r}) + \hat{V}_{pol}(\boldsymbol{r}) + \hat{V}_{rep}(\boldsymbol{r}) \tag{1}$$

where $\hat{T}(\boldsymbol{r})$ is the kinetic energy operator for the excess electron and the operators $\hat{V}_{es}(\boldsymbol{r})$, $\hat{V}_{pol}(\boldsymbol{r})$, and $\hat{V}_{rep}(\boldsymbol{r})$ represent, respectively, the electrostatic, polarization, and

repulsion potential that the excess electron experiences in the presence of the molecule. The molecule is treated as a fixed rigid body and the energy of the excess electron is evaluated on a real space 3D grid of points, $\boldsymbol{r}$, using a sine-type discrete variable representation (DVR) basis [13, 15]. The construction of the sine DVR basis starts from particle-in-a-box (PIB) eigenfunctions of the form,

$$\varphi_m(x) = \begin{cases} \sqrt{\frac{2}{L}} \sin\left(\frac{m\pi\,(x - x_0)}{L}\right) & -\frac{L}{2} \leq x \leq \frac{L}{2} \\ 0 & \text{otherwise} \end{cases} \tag{2}$$

where we represent them in one dimension, x, for simplicity. In equation (2), L is the length of the box, x_0 corresponds to the edge $-L/2$, and m a positive integer. In the case of three dimensions, the wavefunction is a product of sine functions for each Cartesian direction, i.e., $\varphi_{j,k,m}(x, y, z) = \varphi_j(x)\varphi_k(y)\varphi_m(z)$.

The PIB functions given in (2) are eigenfunctions of the kinetic energy operator, but not of the potential energy operators. Discretizing the space in the box into a grid of evenly spaced points $k = 0, 1, \ldots, n+1$, one can form another basis (again represented in one dimension for simplicity),

$$u_j(x) = \sqrt{\frac{L}{n+1}} \sum_{k=1}^{n} \varphi_k(x)\varphi_k^*(x_j) \qquad j = 1, 2, \ldots, n \tag{3}$$

where $k = 0$ and $k = n + 1$ correspond to the edges of the box and x_j refers to the coordinate of a particular grid point. Due to the orthogonality of the PIB eigenfunctions and the applied quadrature rule, the $u_j(x)$ function is peaked at the grid point x_j and is zero at every other grid point. As a result, the potential matrix is diagonal in this representation. The kinetic energy is not diagonal in the $\{u_j(x)\}$ basis, but is given by relatively simple analytical expressions [15].

2.2. Potential Terms

We describe the long-range electrostatic interaction of an electron with a molecule through the use of atomic multipoles. For each atom i, we assign a permanent charge q_i, dipole $\boldsymbol{\mu}_i$, and quadrupole $\bar{\boldsymbol{\Theta}}_i$. This gives the following potential,

$$V_{es}(\boldsymbol{r}) = -\sum_{i=1}^{N} \left(\frac{q_i}{R_{eff}} + \frac{\boldsymbol{\mu}_i \cdot \boldsymbol{R_{ie}}}{R_{eff}^3} + \frac{\boldsymbol{R_{ie}} \cdot \bar{\boldsymbol{\Theta}}_i \cdot \boldsymbol{R_{ie}}}{R_{eff}^5} \right) \tag{4}$$

where N is the number of atoms and $\boldsymbol{R_{ie}} = \boldsymbol{r} - \boldsymbol{R_i}$, i.e. the vector pointing from atom i located at position $\boldsymbol{R_i}$ to the excess electron located at DVR grid point $\boldsymbol{r}$. The atoms are fixed during the simulation so the operator $V_{es}(\boldsymbol{r})$, and all other model Hamiltonian operators for that matter, are denoted as a function of only the excess electron's position $\boldsymbol{r}$. Note that $\boldsymbol{\mu}_i$ is a vector, $\bar{\boldsymbol{\Theta}}_i$ a matrix, and the subscript i designates that the multipoles are centered on atom, i. Short-range divergence in the electron-molecule

electrostatic interaction is avoided by employing a damped distance function of the form [17],

$$R_{eff} = \begin{cases} R_{ie} & R_{ie} \geq d \\ d\left(\frac{1}{2} + \left(\frac{R_{ie}}{d}\right)^3 \left(1 - \frac{R_{ie}}{2d}\right)\right) & R_{ie} < d \end{cases} \tag{5}$$

where R_{ie} is the magnitude of the vector between the electron and an atom. This effective distance damping is applied to the electron-molecule polarization interaction as well. The cutoff distance, d, differs for the electrostatic and polarization interactions, with the values being given in Section 2.3. The same approach has been used in prior studies of NVCB anions of fullerene and water clusters [13–15, 17].

As mentioned previously, $V_{pol}(\boldsymbol{r})$ is based on the Mayer-Åstrand polarization model, in which each atom is assigned an inducible charge and an inducible dipole [50]. The interactions between the inducible moments are damped to avoid divergence in the polarization energy at short distances. Note that this damping only applies to interactions between inducible moments, not the interaction between the excess electron and the inducible moments, which is handled by (5). To determine the induced moments in the model, the polarization energy is minimized subject to the constraint that the total molecular charge is conserved via a Lagrange multiplier.

The inducible charges and dipoles describe the response of the σ and π electrons to an external electric potential and field, polarizing within (charges and dipoles) and out (dipoles) of the molecular plane. The self-induced polarization potential the excess electron experiences at DVR grid point $\boldsymbol{r}$ is,

$$V_{pol}(\boldsymbol{r}) = -\frac{1}{2}\left(\boldsymbol{F}^{\mathrm{e}}(R_{eff})\right)^{\mathrm{T}} \cdot \bar{\boldsymbol{\alpha}}_{pol} \cdot \boldsymbol{F}^{\mathrm{e}}(R_{eff}) \tag{6}$$

where $\boldsymbol{F}^{\mathrm{e}}(R_{eff})$ is a supervector containing the potential and electric field of the excess electron at all atomic positions as well as the Lagrange multiplier used to conserve charge. The molecular polarization matrix, $\bar{\boldsymbol{\alpha}}_{pol}$, contains the damped local interactions between induced multipoles, and is obtained via the following inverted matrix:

$$\bar{\boldsymbol{\alpha}}_{pol} = \begin{pmatrix} \mathbf{T}_{\mathrm{q-q}} & -\mathbf{T}_{\mathrm{q-p}} & \mathbf{1} \\ -\mathbf{T}_{\mathrm{p-q}} & -\mathbf{T}_{\mathrm{p-p}} & \mathbf{0} \\ \mathbf{1} & \mathbf{0} & 0 \end{pmatrix}^{-1} \tag{7}$$

The entries $\mathbf{T}_{\mathrm{q-q}}$, $\mathbf{T}_{\mathrm{p-p}}$, $\mathbf{T}_{\mathrm{q-p}}$, and $\mathbf{T}_{\mathrm{p-q}}$ are tensor matrices containing the damped charge-charge, dipole-dipole, charge-dipole, and dipole-charge interaction equations respectively. Their dimensions are N × N, 3N × 3N, 3N × N, and N × 3N, respectively. The entries $\mathbf{1}$ and $\mathbf{0}$, represent a vector of ones of length N and of zeros of length 3N, respectively. The vector of ones is included to ensure that the overall charge of the system is constrained to be zero. Summing up the atomic contributions in $\bar{\boldsymbol{\alpha}}_{pol}$ yields the familiar 3×3 molecular polarizability matrix $\bar{\boldsymbol{\alpha}}_{mol}$.

The Mayer-Åstrand method presumes that atomic charge densities are well described by Gaussian distributions. This yields three free parameters for the atomic

inducible moments: the charge width (R_q) which is related to chemical hardness and affects induced charges, the in-plane ($\alpha_\parallel$), and out-of-plane ($\alpha_\perp$) atomic dipole polarizabilities. There is a term for the dipolar width (R_p) of an atomic charge distribution in the Mayer-Åstrand model employed in the damping of the dipole-dipole, charge-dipole, and dipole-charge interactions. In their model, R_p is defined in terms of the atomic polarizability components $\alpha_\parallel$ and $\alpha_\perp$ in the following equation expressed in a.u. [50]:

$$R_p = \left(\sqrt{\frac{2}{\pi}} \left(2/\alpha_\parallel + 1/\alpha_\perp \right)^{-1} \right)^{1/3} \tag{8}$$

When fitting the parameters in the model to reproduce the static dipole polarizabilties obtained from electronic structure calculations, we found that when using this definition of R_p, we could accurately reproduce the MP2 and PBE0 in-plane polarizabilities but underestimated the out-of-plane polarizabilities by as much as 19%. To address this limitation, we made the R_p of the carbon atoms a free parameter allowing it to vary along with the three other parameters for the carbon atoms, R_q, $\alpha_\parallel$, and $\alpha_\perp$. This relaxation of the Mayer-Åstrand model was found to produce better molecular polarizabilties. The process for fitting all four parameters is detailed in section 2.3.

The potential capturing the short-range interactions, not described through the permanent multipoles and the polarization potential, of the excess electron with the atoms is of the form,

$$V_{rep}(\boldsymbol{r}) = \sum_{i}^{\mathrm{N}} a \exp\left(-bR_{ie}^2\right) \tag{9}$$

where the sum runs over each atom, i, in the molecule. In this work, the same parameters a and b are used for both C and H. The value of b was carried over from previous work on fullerene structures and the process by which it was determined can be found in the SI of reference [13]. The coefficient a was obtained by reproducing the EBE Voora and Jordan obtained for circumcoronene [29]. The resulting repulsive potential accounts for the orthogonalization between the orbital occupied by the excess electron and the filled orbitals of the molecule. Additionally, charge penetration and exchange effects are implicitly folded into the potential.

2.3. Calculation Details

In this section, we describe the procedures used to parameterize the potentials of the one-electron model Hamiltonian described in section 2.2 and the QM calculations performed to measure the model results against. However, the entire parameterization process is summarized in figure 1 for the convenience of the reader.

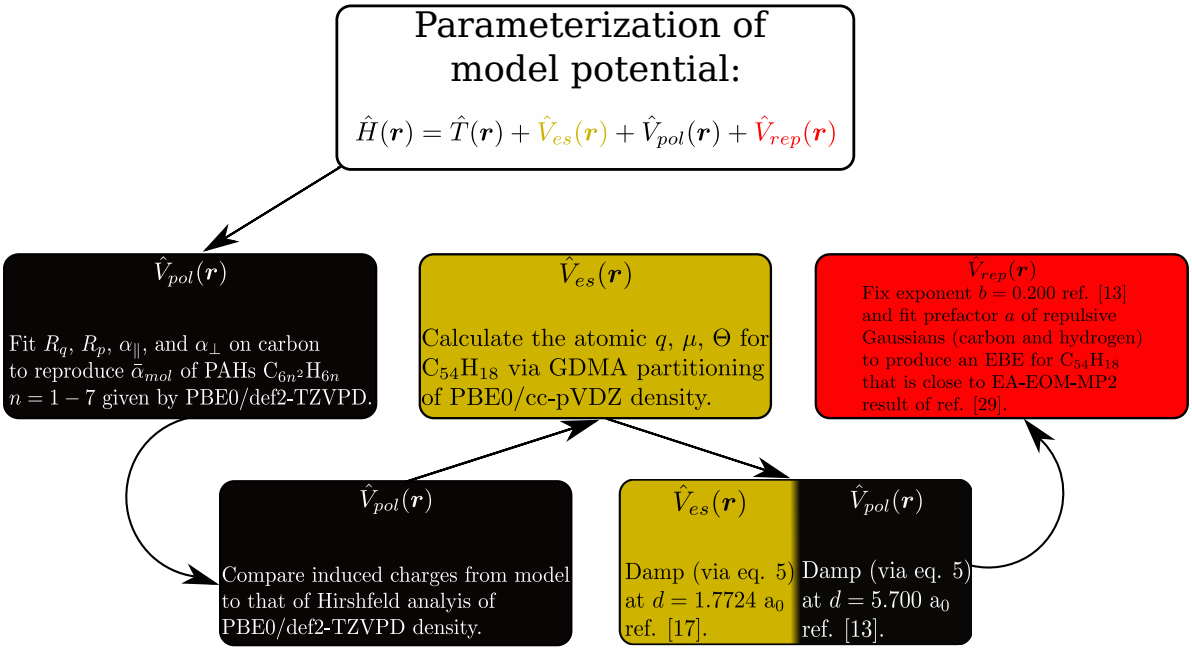

Figure 1: Summary of parameterization process for the model Hamiltonian. The process flows from the top box to the various steps as indicated by the arrows.

The systems studied in this work are hexagonal PAHs in the $C_{6n^2}H_{6n}$ (n = $1, 2, 3, \ldots$) series. The sp^2 carbon network is modeled after graphene (C-C bonds = 1.42 Å and C-C-C angles = 120°) [60]. Dangling C-C bonds present at the edges of the carbon nanoflakes were capped with hydrogen for the PAHs (C-H bonds = 1.09 Å and C-C-H angles = 120°).

In section 3.1 we compare the in-plane ($\alpha_{xx/yy}$) and out-of-plane (α_{zz}) components of the static dipole polarizability obtained from the model to the results of PBE0, HF, MP2, and CAM-B3LYP calculations. The polarizabilities were obtained for the full series of PAHs considered using HF and PBE0, while MP2 and CAM-B3LYP results are reported for only the first four members, C_6H_6 to $C_{96}H_{24}$. These calculations were performed in Psi4 v 1.4a2 or v 1.3.2 with default convergence criteria [61–63]. To avoid linear dependency issues, symmetry-adapted, orthogonal combinations of atomic orbitals with overlap eigenvalues smaller than 10^{-7} were discarded. The def2-TZVPD orbital basis was used as it is optimized explicitly for dipole polarizabilities, is moderately diffuse, and is designed to scale well with large molecular systems without introducing significant linear dependence [64]. The Coulomb-exchange (JK) integrals were density fit in the SCF calculations with the def2-TZVP JK-fitting basis, which is also referred to as the def2-universal-JK fitting basis set in the literature [65]. The integral transformations for the MP2 calculations used the def2-TZVPD resolution of identity fitting (RI a.k.a. MP2-fitting) basis [66]. For the PAHs $C_6H_6 - C_{150}H_{30}$, the polarizabilities were obtained via a five-point stencil, first-order central difference of the induced dipole with a step size of ±0.001 a.u. in the electric field strength. For the last two members, $C_{216}H_{36}$ and $C_{294}H_{42}$, a three point stencil first-order central difference of the induced dipole with a

step size of ±0.002 a.u. was used. The molecules were oriented such that the largest Abelian subgroup symmetry could be used in the presence or absence of an electric field perturbation: D_{2h} when no field was applied and C_{2v} when a field was applied along the x, y, or z axis. Figures 2a–2c illustrate the orientation for the first three members of the PAH series.

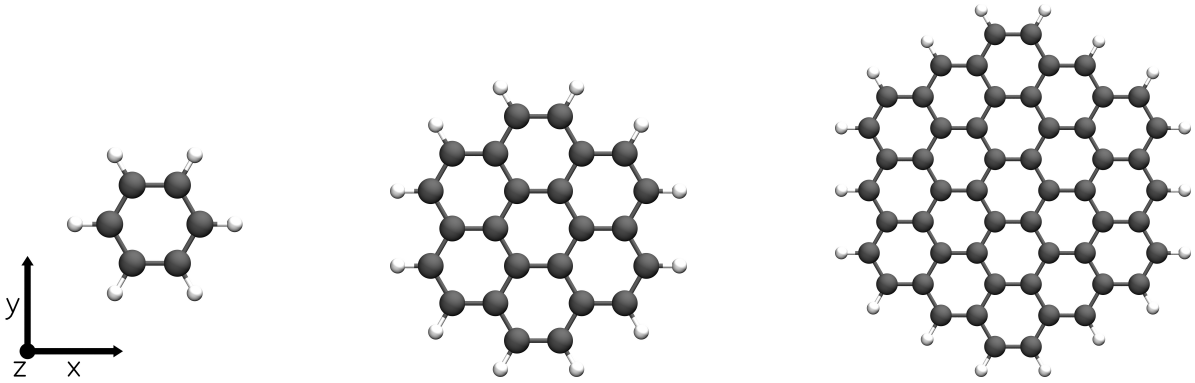

(a) C_6H_6 **(b)** $C_{24}H_{12}$ **(c)** $C_{54}H_{18}$

Figure 2: Orientation of molecules with respect to the axes along which electric fields are applied in static dipole polarizability calculations. The x and y axes correspond to C_2 rotational axes and the z-axis to the principal C_6 rotational axis. The molecules are centered on the origin. Image generated using VMD [67]

Within our model the carbon atom's charge flow parameter, R_q, atomic inducible dipole parameters, $\alpha_\parallel$ and $\alpha_\perp$, and dipole width, R_p, were fit to reproduce the PBE0/def2-TZVPD static dipole polarizability tensors for the series of PAHs, C_6H_6 to $C_{294}H_{42}$. The fitting process went as follows:

(i) Fit $\alpha_\perp$ and R_p to the out-of-plane component, α_{zz}, from PBE0/def2-TZVPD.

(ii) Fix $\alpha_\perp$ and R_p from the previous step and fit $\alpha_\parallel$ and R_q to the in-plane components, $\alpha_{xx/yy}$, from PBE0/def2-TZVPD.

Steps (i) and (ii), were performed by using the non-linear least squares module, `least_squares`, of the SciPy Python library to minimize the sum of the residual errors between the model and PBE0 polarizability components [68]. This yielded the following parameters $R_q = 0.4469$ a_0, $R_p = 1.6855$ a_0, $\alpha_\parallel = 10.1137$ a_0^3, and $\alpha_\perp = 13.6586$ a_0^3 for the carbon atoms. For the H atoms the isotropic dipole polarizabilities, $\alpha_\parallel = \alpha_\perp = 3.0172$ a_0^3 and $R_p = 0.9293$ a_0, developed by Mayer and Åstrand were used without further optimization [50]. Also, charge flow was not permitted to or from the H atoms. To further assess whether or not the value of R_q was appropriate, we compared the induced charges obtained from the model for $C_{54}H_{18}$ to a Hirshfeld analysis [69] of the PBE0/def2-TZVPD charge density when a uniform field of strength of 0.001 a.u. was applied along the x or y axis. The induced charges from the model were found to be in reasonable agreement with that of the Hirshfeld analysis, which was performed using Gaussian 16 [70]. This parameter set was used to calculate the dipole polarizability

components of the PAH series $C_6H_6 - C_{294}H_{42}$. To determine the primary contributions to the in-plane ($\alpha_{xx/yy}$) polarizability the model calculations were performed using charge flow alone, inducible dipoles alone, and the combination of the two.

To assess the accuracy of the polarization model and the suitability of the parameter set, comparisons are made between the model, PBE0, and MP2 polarization potentials for $C_6H_6 - C_{96}H_{24}$ in section 3.2. HF values are also reported to allow for an assessment of the importance of correlation effects for the polarizabilities. In one set of calculations a point charge, Q = −1 e, was scanned above the center of the innermost carbon ring at distances of $z = 6.0 - 20.0$ a_0 with a step size of 2.0 a_0. In a separate set of calculations, the point charge was scanned within the molecular plane (xy) along the x-axis at distances of $x = 6.0 - 20.0$ a_0 from the edge of the PAH with a step size of 2.0 a_0. The MP2 scan proved to be expensive for the largest PAH, $C_{96}H_{24}$, so for this system only four distances in the scan along z and x were evaluated: 6.0, 10.0, 14.0, and 18.0 a_0. For even members in the PAH series (n = 2 : $C_{24}H_{12}$ and n = 4 : $C_{96}H_{24}$), the point charge traces a line that bisects the space between two hydrogen atoms capping the edges, while for odd members (n = 1 : C_6H_6 and n = 3 : $C_{54}H_{18}$) it approaches a hydrogen atom. For the electronic structure methods, the polarization potential was evaluated using the following formula,

$$V_{pol}(R) = E^{Q+PAH}(R) - V_{es}^{PAH}(R) - E^{PAH} \tag{10}$$

where $E^{Q+PAH}(R)$ is the single point energy of a PAH in the presence of the point charge, Q, fixed at distance R along x or z, $V_{es}^{PAH}(R)$ is the electrostatic potential of the PAH at R, and E^{PAH} is the single point energy of the isolated PAH. We subtract $V_{es}^{PAH}(R)$ as Q is negative point charge representing an excess electron. Figures 3a and 3b shows the axes along which the point charge is located for the first two members in the PAH series.

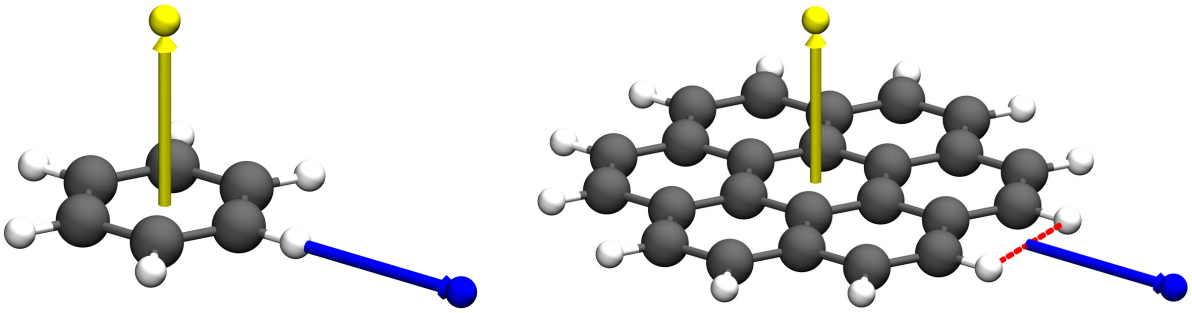

(a) C_6H_6 **(b)** $C_{24}H_{12}$

Figure 3: Depiction of point charge and acene arrangement in polarization scans for C_6H_6 and $C_{24}H_{12}$. The yellow and blue spheres indicate the placement of the point charge at a distance of 6.0 a_0 and the arrows point from the origin to the point charge, illustrating how the distance is measured. The blue arrow and sphere represent the scans where the point charge is coplanar and the yellow set represents the scans perpendicular to the plane of atoms. The dashed red line between the hydrogen atoms of $C_{24}H_{12}$ provides a visual indication of the origin from which x is measured for the coplanar scans of even members. The coplanar scans align with a C_2 rotational axis and the perpendicular scans align with the C_6 rotational axis. Image generated using VMD [67]

In sections 3.3 and 3.4 we evaluate the success of the model in predicting the EBE of the lowest energy NVCB anion of the PAHs. In section 3.3 we evaluate the quality of the one-electron model when electrostatics and repulsion are introduced using a model system. Circumcoronene, $C_{54}H_{18}$, is the smallest hexagonal PAH in the series $C_{6n^2}H_{6n}$ for which Voora and Jordan identified a bound NVCB state [29]. However, with a slight enhancement of nuclear charges coronene, $C_{24}H_{12}$, can be made to possess a bound non-valence anion. Nuclear-charge stabilization has been used in studies of the temporary (unbound) anions of N_2^- [71, 72], the temporary polyanions of doubly- and triply-deprotonated naphthalenes [73], and the metastable dianion SO_4^{2-} [74]. Coronene is a computationally tractable system affording treatment with both EA-EOM-MP2 and EA-EOM-CCSD. This provides an additional data point for assessing the performance of the model. We employed the modified Roos-ANODZ [75] basis from Voora and Jordan's study with frozen core orbitals, denoted as C (4s2p1d) , H (4s3p) , GH (6s6p3d) /5Å in their work [29]. This basis includes a set of diffuse 6s, 6p, and 3d basis functions on ghost atoms 5Å above and below the central ring of coronene, which is denoted by GH (6s6p3d) /5Å. Binding energies were obtained using EA-EOM-MP2 and EA-EOM-CCSD at six nuclear scaling factors: 1.000125, $1.0001\bar{6}$, $1.000208\bar{3}$, 1.00025, $1.000291\bar{6}$, and $1.000\bar{3}$. These scale factors correspond to excess molecular charges of 0.0195, 0.0260, 0.0325, 0.0390, 0.0455, and 0.0520 e, respectively. These calculations were performed using the CFOUR v2.1 package [76].

Due to the enhanced nuclear charges, $C_{24}H_{12}$ also possesses Rydberg states. If a sufficiently flexible basis set is used in the HF step of the EOM calculations, these appear as bound virtual orbitals, i.e. they are bound in the Koopmans' theorem (KT) approximation [77]. We show in section 3.3 that with the inclusion of electron correlation

through the EOM procedure the lowest energy solution corresponds to the desired non-valence anion rather than a Rydberg state. Moreover, rather than presenting a problem, the presence of Rydberg states can be used as another performance check for the model Hamiltonian. Namely, comparison of the EBE predicted by the model without the contribution of polarization ($V_{rep,es}$) to the ab initio KT result, provides a test of the performance of the electrostatic and repulsive potential terms in the model Hamiltonian. However, even with the supplemental GH functions the modified Roos-ANODZ described in the previous paragraph, is not adequate for describing the highly extended Rydberg levels for the nuclear charges employed. Thus, the KT EBE values we report in this work were obtained using an even more diffuse 7s4p GH sets of functions, with s exponents as small as 0.0001105 for the two floating centers [78]. These highly diffuse functions prove relatively unimportant for the lowest energy eigenvalue in the EA-EOM calculations, which is more strongly bound and more localized than the Rydberg states as described by the KT approximation.

Following the charge-scaled coronene calculations, we report in section 3.4 the binding energies for the lowest energy NVCB state of acenes $C_{54}H_{18}$ to $C_{294}H_{42}$. In all model calculations of the EBEs a common set of model parameters were employed, which are detailed here. The atomic charge and dipolar widths (R_q and R_p) and dipole polarizability ($\alpha_{\parallel}$ and $\alpha_{\perp}$) parameters given earlier in this section were used to model the polarization of the PAHs in response to an excess electron. The cutoff for damping the interaction of the excess electron with inducible atomic multipoles, see equation (5), was set to $d = 5.70$ a_0, which was taken from a previous study on fullerenes [13]. To describe the short-range repulsive interactions between the excess electron and atoms via equation (9), the same coefficient, $a = 0.22705$, and exponential factor, $b = 0.200$, were used for the repulsive Gaussians on carbon and hydrogen atoms. To model the long-range electrostatic potential (V_{es}) of the PAHs, permanent atomic charges, dipoles, and quadrupoles were obtained via Gaussian distributed multipole analysis (GDMA) [79] of the PBE0/cc-pVDZ charge density [80] calculated using Gaussian 16 [70]. For $C_{24}H_{12}$ the atomic charges from GDMA were modified to replicate the excess molecular charge present in the charge stabilized KT and EOM calculations described in the previous two paragraphs. For the larger PAHs considered, $C_{54}H_{18}$ to $C_{294}H_{42}$, the nuclear charges were not enhanced. For both the charge-scaled coronene and charge-neutral PAH model calculations of EBE, the cutoff for damping the interaction of the excess electron with electrostatic atomic multipoles, see equation (5), was set to $d = 1.7724$ a_0, which came from reference [17].

For the charge-scaled coronene calculations, the DVR box length was set to $L = 402$ a_0 containing a $200 \times 200 \times 200$ grid of points yielding a spacing of 2 a_0 between points. Section 3.3 reports the model binding energies for $C_{24}H_{12}$ at all nuclear scale factors using the full ($V_{pol,rep,es}$) and the repulsion and electrostatic ($V_{rep,es}$) components of the one-electron model Hamiltonian. A box length of $L = 402$ a_0 was selected in this set of calculations to prevent artificial confinement of the highly extended Rydberg state wavefunction at the lowest values of nuclear charge scaling and in the absence of

model polarization ($V_{rep,es}$). In the calculations modeling charge-neutral PAHs, $C_{54}H_{18}$ to $C_{294}H_{42}$, we used a DVR box with side length L = 251 a_0 containing a $250 \times 250 \times 250$ grid of points yielding a spacing of 1 a_0 between points. This DVR box and grid size was selected to assure that the EBE of $C_{54}H_{18}$, with the most weakly bound NVCB anion, was well converged. Going to a larger DVR box length (L = 301 a_0) with a 1 a_0 grid spacing, modified the binding of $C_{54}H_{18}$ by 0.03 meV. In section 3.4, the model binding energies for PAHs $C_{54}H_{18}$ to $C_{294}H_{42}$ are reported for the model Hamiltonian with polarization alone (V_{pol}), with both polarization and repulsion ($V_{pol,rep}$), and the full potential ($V_{pol,rep,es}$).

Having validated the model potential components and their parameterization in the preceding sections, we explore the edge localization of the lowest energy NVCB anion of the charge-neutral PAHs. In section 3.5, we plot one-dimensional slices of the interaction energy for $C_{54}H_{18}$ and $C_{294}H_{42}$. These slices were obtained by scanning the energy at DVR grid points along the x axis at a fixed vertical separation, z, above the molecular plane. To gain an understanding of the role various potential components play in the binding of an excess electron in the charge-neutral PAHs, we plot slices of the individual model potential components, V_{es}, V_{rep}, and V_{pol}, and the combinations $V_{pol,rep}$, and $V_{pol,rep,es}$. To illustrate the impact of electrostatics on the charge density of the NVCB anions, we plot the difference in the excess electron density due to electrostatics in the model: $\Delta\rho(V_{es}) = \rho(V_{pol,rep,es}) - \rho(V_{pol,rep})$ in section 3.5. The density differences were calculated using Multiwfn v3.7 [81]. The isosurfaces are plotted for all charge-neutral PAHs studied at isovalues that correspond to 90% enclosure of $\Delta\rho(V_{es})$.

3. Results & Discussion

3.1. Model Validation: Polarizabilities

Accurately modeling the polarization response of the PAHs to an external electric field is the most important step in building a one-electron model for NVCB anions as it effectively accounts for the dispersion-type correlation responsible for stabilizing NVCB states. The polarization response of a molecule in the one-electron model is described via inducible atomic charges and dipoles. Methods employing charge equilibration techniques run the risk of overpolarizing molecules. This has been characterized in systems with insulating properties by an erroneous superlinear scaling of static dipole polarizability with system size [53, 55]. To establish the performance of the model, the in-plane and out-of-plane components of model and QM dipole polarizabilities are compared in figures 4a and 4b for PAHs $C_6H_6 - C_{294}H_{42}$.

There are clear trends for the in-plane, $\alpha_{xx/yy}$, and out-of-plane, α_{zz}, components of the polarizability as the number of carbon atoms, N_C, increases. The in-plane polarizability scales essentially quadratically with system size for all QM methods as well as the polarization model when charge flow is included. On the other hand, the out-of-plane polarizability exhibits, roughly, a linear scaling with system size for all

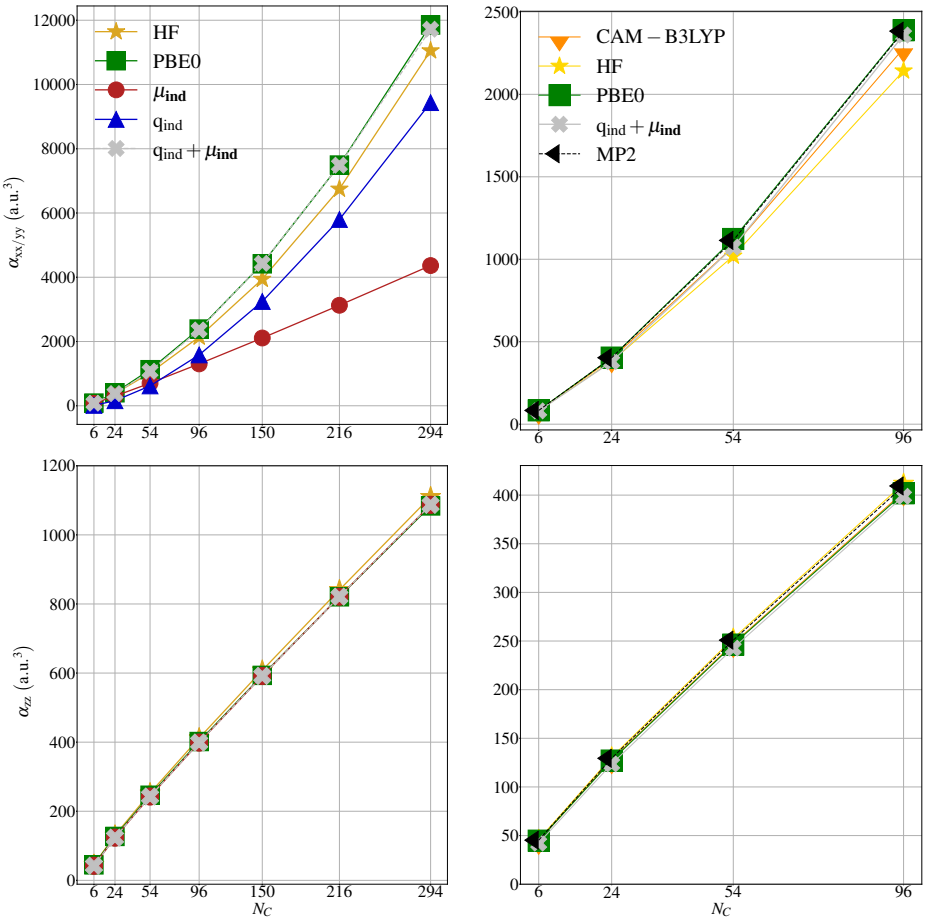

(a) $C_6H_6 - C_{294}H_{42}$ **(b)** $C_6H_6 - C_{96}H_{24}$

Figure 4: In-plane ($\alpha_{xx/yy}$) and out-of-plane (α_{zz}) components of the static dipole polarizability (a.u.^{3}) for PAHs $C_{6n^2}H_{6n}$, n = 1 − 7, vs. the number of carbon atoms, N_C. The images on the left (a) report results obtained with the polarization model including induced charges only q_{ind}, dipoles only $\boldsymbol{\mu}_{ind}$, and coupled induced charges and dipoles $q_{ind} + \boldsymbol{\mu}_{ind}$, as well as the results of HF and PBE0 calculations. The images on the right (b) compare the polarizabilities from the full model with the results of HF, MP2, PBE0, and CAM-B3LYP calculations on the PAHs up to n = 4. Lines between points do not reflect fitted functions and are included for tracking trends in the data. Images generated using Matplotlib [82].

methods considered. When considered individually, the point inducible dipole ($\boldsymbol{\mu}_{ind}$) and the charge flow (q_{ind}) contributions to the model $\alpha_{xx/yy}$ become nearly equal for $C_{54}H_{18}$, with the charge flow contribution growing more rapidly with increasing system size. The net in-plane polarizability predicted by the full model ($q_{ind} + \boldsymbol{\mu}_{ind}$) is less than the sum of the induced dipole and charge flow contributions when calculated separately due to the cross terms, $\mathbf{T}_{q-p}$ and $\mathbf{T}_{p-q}$, that couple the inducible dipole and charge-flow terms. A superlinear scaling of the in-plane component of hexagonal PAHs was observed in past work by Kirtman et al. [57]. Different scaling for in-plane and out-of-plane polarizabilities has been observed in one-dimensional polyenes and linear acenes

[83], as well as polythiophenes [84]. The quadratic scaling of the in-plane components with system size indicates a growing conductive behavior brought about by electron delocalization within the π system [83]. The inclusion of charge-flow polarization in the model is crucial for capturing the increasing delocalization of π electrons in the PAHs and concomitant growth in $\alpha_{xx/yy}$.

We now examine in more detail the polarizabilities obtained by the various QM methods. The $\alpha_{xx/yy}$ components obtained via methods including electron correlation (PBE0, CAM-B3LYP, and MP2) grow with molecular size somewhat faster than those obtained via HF. The CAM-B3LYP values are slightly smaller than those from PBE0 and MP2. For α_{zz}, all methods considered give similar values. The agreement between the in-plane polarizabilities obtained from MP2 and PBE0 is surprising, since Kirtman et al. evaluated the $\alpha_{xx/yy}$ components of the dipole polarizability for hexagonal PAHs (n = 1 − 5) with B3LYP, MP2, and HF and found that the B3LYP values grew faster with system size than those from MP2 calculations [57]. The authors calculated the ratio of $\alpha_{xx/yy}$ given by B3LYP to that of MP2 for $C_{96}H_{24}$ and obtained 1.0615. In the present study, the same ratio for PBE0 relative to MP2 is 1.0021. In fact, the ratio $\alpha_{xx/yy}$(PBE0/MP2) from our calculations is less than 1.01 for all PAHs studied with MP2. Additionally, we calculated the polarizability for $C_{96}H_{24}$ with B3LYP and found that $\alpha_{xx/yy}$(B3LYP/MP2) = 1.0150, which is an appreciably smaller ratio than that obtained by Kirtman et al. We attribute this discrepancy to the fact that our calculations employed a much more flexible basis set than 3-21G [85], which was used by Kirtman et al.

The close agreement of the MP2 and PBE0 polarizabilities indicates that either method can be used as a reference for assessing the model polarizabilities. When both inducible atomic charges and dipoles are used in the model, $q_{ind} + \boldsymbol{\mu}_{ind}$, the polarizabilities are in good agreement with the PBE0 and the MP2 results. For $\alpha_{xx/yy}$, the largest discrepancy between the model and the correlated ab initio results occurs for corenene, for which the value predicted by the model is underestimated by $\sim 6\%$. For α_{zz}, the largest discrepancy in the model occurs for benzene with an underestimation of $\sim 7\%$ relative to MP2 and $\sim 6\%$ relative to PBE0. The trends in how the polarizabilities evolve with increasing size of the PAH vary slightly for the model, PBE0, and MP2 methods, so there are PAHs for which the model overestimates or underestimates the reference values. However, the magnitude of the absolute errors are small relative to the size of $\alpha_{xx/yy}$ and α_{zz}. These results indicate that the current model is sufficient for the qualitative/semi-quantitative explorations performed in this work.

3.2. Model Validation: Polarization

Next, we evaluate how well the model reproduces the polarization potential for a negative point charge interacting with the PAHs. We first consider the polarization potential when a point charge is scanned along the principal rotation axis of the PAHs. Figure 5 shows the results for the PAHs C_6H_6 to $C_{96}H_{24}$.

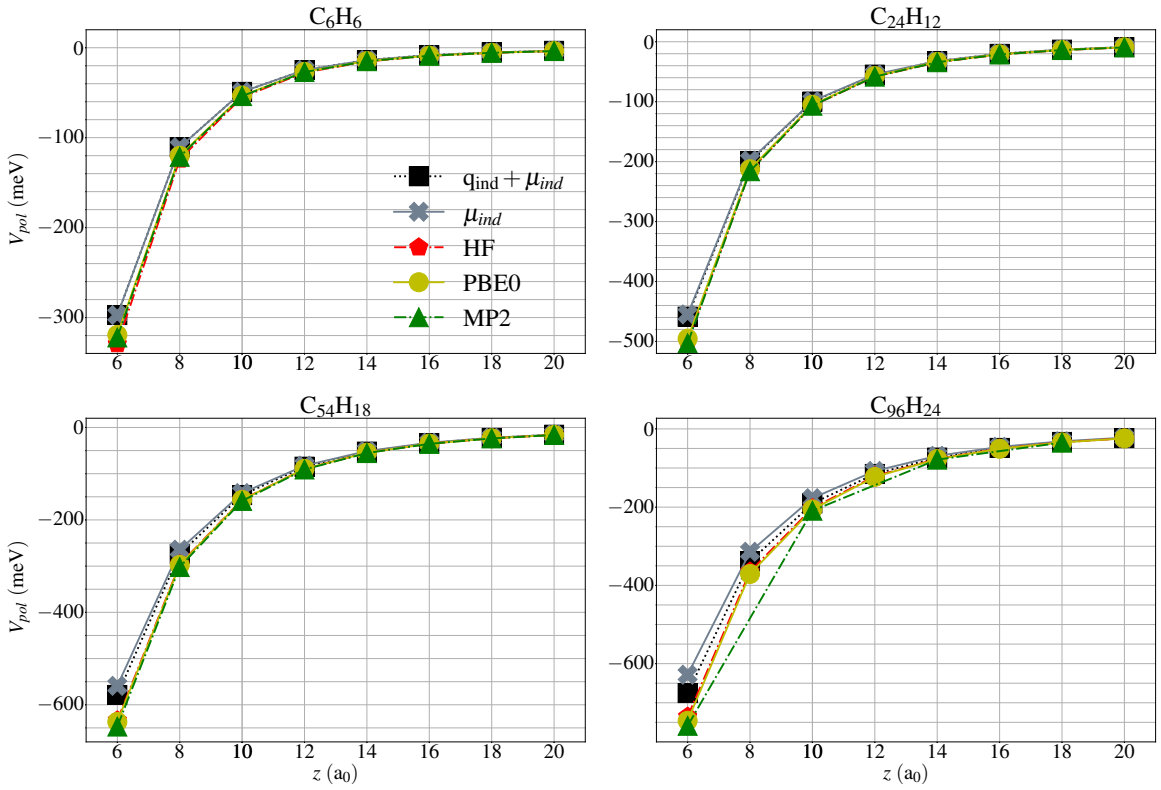

Figure 5: Polarization potential (meV) for a point charge (Q = −1 e) at a distance of z (a_0) along the C_6 rotational axis of PAHs $C_{6n^2}H_{6n}$ (n = 1 − 4). Results are shown for HF, PBE0, and the polarization model. Model results are shown for V_{pol} using induced dipoles only, $\boldsymbol{\mu}_{\text{ind}}$, as well as coupled induced charges and dipoles, $q_{\text{ind}} + \boldsymbol{\mu}_{\text{ind}}$. Lines between points do not reflect fitted functions and are included for tracking trends in the data. Images generated using Matplotlib [82].

The polarization model closely reproduces the PBE0 and MP2 values of the polarization potential along the principal rotational axis except at short separations from the plane of the molecule. An interesting point of note is that the HF polarization potential tracks closely with those from the PBE0 and MP2 calculations as well. However, on the scale of the figure it is difficult to ascertain the percentage deviation of the model potential results from those obtained via electronic structure calculations at long-range. Table 1 reports the deviation of the model potential results from those of the HF, MP2, and PBE0 calculations by providing the percent changes.

From table 1 it is seen that in the case of a point charge approaching along the principal rotational axis, the model underestimates the magnitude of the polarization potential for all PAHs at all distances considered. The discrepancies between the model and PBE0 results are the largest at small point-charge PAH separations $z < 10$ where the percent changes relative to PBE0 vary from −9.5 to −6.2% and for MP2 they vary from −11 to −7.6%. At longer range $z \geq 10$, the percent changes are somewhat smaller ranging from −7.9 to −2.8% relative to PBE0 and from −8.9 to −4.1% relative to

Table 1: Percentage change of the $q_{ind} + \boldsymbol{\mu}_{ind}$ polarization potential relative to HF, PBE0[a], and MP2[b] for a point charge (Q = −1 e) at a distance z (a_0) along the C_6 rotational axis of PAHs $C_{6n^2}H_{6n}$ (n = 1 − 4).

z	C_6H_6	$C_{24}H_{12}$	$C_{54}H_{18}$	$C_{96}H_{24}$
6	−9.8 [−6.9] (−7.7)	−8.4 [−7.4] (−8.8)	−8.7 [−9.2] (−10.6)	−8.2 [−9.5] (−11.0)
8	−10.9 [−8.0] (−8.8)	−7.4 [−6.2] (−7.6)	−7.6 [−8.1] (−9.4)	−7.1 [−8.6] (—)[c]
10	−10.8 [−7.9] (−8.7)	−6.4 [−5.1] (−6.5)	−6.3 [−6.6] (−7.9)	−5.9 [−7.4] (−8.9)
12	−10.4 [−7.6] (−8.4)	−5.9 [−4.4] (−5.7)	−5.3 [−5.3] (−6.7)	−4.8 [−6.2] (—)
14	−10.0 [−7.4] (−8.0)	−5.7 [−3.9] (−5.3)	−4.5 [−4.4] (−5.7)	−4.1 [−5.2] (−6.7)
16	−9.5 [−7.0] (−7.9)	−5.5 [−3.7] (−5.0)	−4.1 [−3.7] (−5.0)	−3.5 [−4.4] (—)
18	−9.4 [−6.8] (−7.7)	−5.4 [−3.5] (−4.8)	−3.8 [−3.2] (−4.6)	−3.0 [−3.7] (−5.2)
20	−8.9 [−6.9] (−7.6)	−5.3 [−3.4] (−4.8)	−3.6 [−2.8] (−4.1)	−2.7 [−3.2] (—)

[a] Percent change relative to PBE0 is in square brackets.

[b] Percent change relative to MP2 is in parentheses.

[c] — indicates that this reference value was not calculated.

MP2. When one considers the change in the in-plane charge distribution induced by a point charge located on the principal rotational axis, one sees that the leading induced molecular moment is the quadrupole, suggesting that to obtain better agreement with the results of the electronic structure calculations it may be necessary to extend the model to include atomic inducible quadrupole polarizabilities.

Figure 6, reports polarization potentials for the same systems when the point charge is coplanar with the molecule and scanned along a C_2 rotational axis (see figures 3a and 3b for visual depictions of the geometries).

In this case, the model yields a potential that is more attractive than any of the QM methods at short range. At long range, the model underestimates the polarization potential from the PBE0 calculations and this is also true with respect to MP2 except for $C_{96}H_{24}$. The HF method tends to give a weaker in magnitude polarization potential than the model and correlated methods at all values of x with the exception of $C_{96}H_{24}$ where HF is slightly more polarized than MP2 at distances of $x = 6$ and 10 a_0. As the system size grows, the separation between the $q_{ind} + \boldsymbol{\mu}_{ind}$ and $\boldsymbol{\mu}_{ind}$ model polarization potentials grows. This coincides with the trends in the $\alpha_{xx/yy}$ values given by q_{ind} and $\boldsymbol{\mu}_{ind}$ seen in figure 4a, where the contribution of charge flow increases more rapidly with system size. The percentage changes between the polarization potential from $q_{ind} + \boldsymbol{\mu}_{ind}$ and the QM methods are tabulated in table 2.

In general, the percentage discrepancies of the model potential results relative to PBE0 and MP2 are smaller in magnitude than what was observed for the scan along the C_6 rotational axis. The percent change relative to PBE0 ranges from −4.6 to 1.2% at long range. A similar trend is observed for the percent change relative to MP2, albeit with a larger span of, −4 to 4.1% at long range. At the shortest distances considered, there is a growing discrepancy between the PBE0 and MP2 values of the in-plane polarization potential with increasing size of the PAH, with the MP2 value being

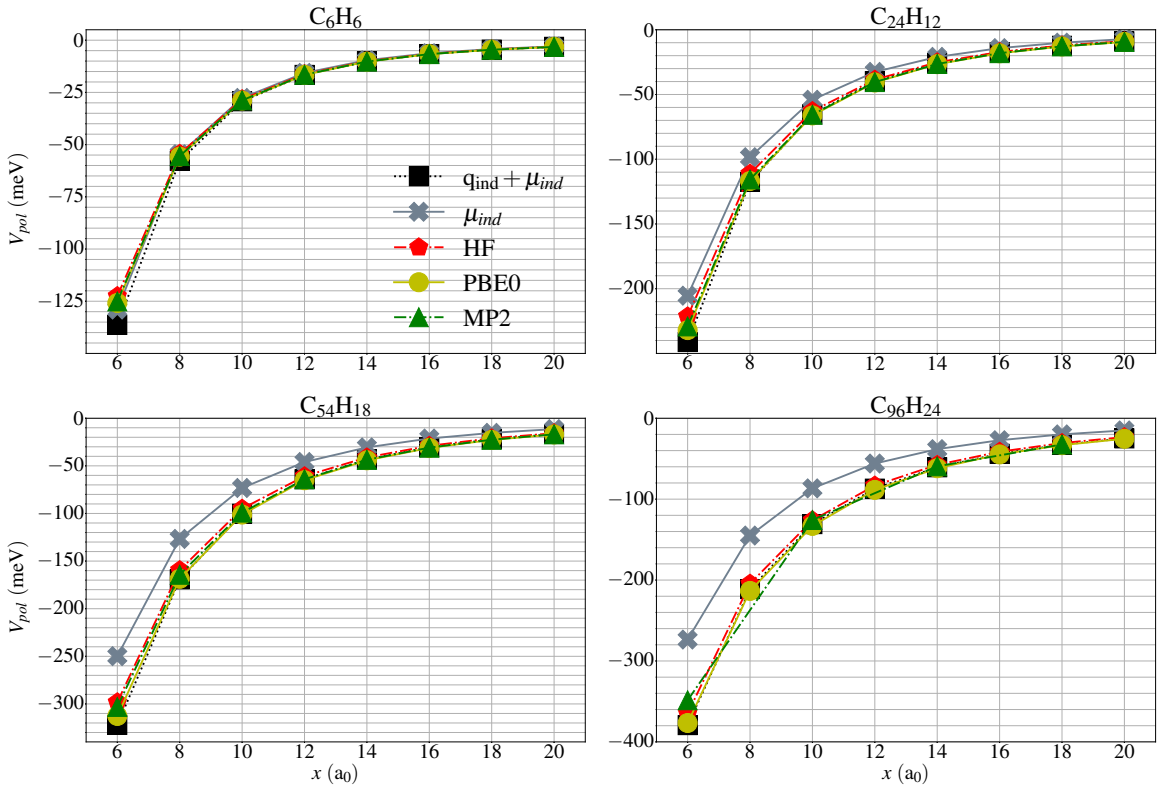

Figure 6: Polarization potential (meV) for a point charge (Q = −1 e) at a distance x (a_0) along a C_2 rotational axis of PAHs $C_{6n^2}H_{6n}$ (n = 1 − 4). Results are shown for HF, PBE0, MP2, and the polarization model. Model results are reported for V_{pol} using induced dipoles only, $\boldsymbol{\mu}_{\text{ind}}$, as well as the full model with coupled induced charges and dipoles, $q_{\text{ind}} + \boldsymbol{\mu}_{\text{ind}}$. Lines between points do not reflect fitted functions and are included for tracking trends in the data. Images generated using Matplotlib [82].

Table 2: Percentage change of $q_{\text{ind}} + \boldsymbol{\mu}_{\text{ind}}$ polarization potential relative to those from HF, PBE0[a], and MP2[b] calculations for a point charge (Q = −1 e) at a distance x (a_0) along one of the C_2 rotational axis of PAHs $C_{6n^2}H_{6n}$ (n = 1 − 4).

x	C_6H_6	$C_{24}H_{12}$	$C_{54}H_{18}$	$C_{96}H_{24}$
6	11.3 [8.4] (9.0)	9.0 [4.0] (5.3)	8.0 [3.0] (6.2)	3.9 [0.7] (8.8)
8	6.2 [3.6] (4.1)	5.8 [0.6] (1.7)	6.1 [0.3] (2.9)	3.3 [−1.1] (—)[c]
10	3.6 [1.2] (1.7)	4.1 [−1.2] (−0.4)	5.5 [−0.9] (1.1)	3.8 [−1.6] (4.1)
12	2.2 [−0.2] (0.3)	3.1 [−2.5] (−1.7)	5.3 [−1.6] (0.0)	4.6 [−1.8] (—)
14	1.2 [−0.9] (−0.6)	2.3 [−3.3] (−2.7)	5.3 [−2.0] (−0.8)	5.4 [−1.8] (2.1)
16	0.6 [−1.4] (−1.0)	1.8 [−3.8] (−3.3)	5.2 [−2.3] (−1.3)	6.1 [−1.7] (—)
18	0.3 [−2.1] (−1.5)	1.4 [−4.3] (−3.7)	5.3 [−2.6] (−1.7)	6.7 [−1.6] (1.0)
20	−0.2 [−1.9] (−1.9)	1.3 [−4.6] (−4.0)	5.3 [−2.8] (−2.0)	7.2 [−1.6] (—)

[a] Percent change relative to PBE0 is in square brackets.

[b] Percent change relative to MP2 is in parentheses.

[c] — indicates that this reference value was not calculated.

about 7.5% smaller in magnitude than the PBE0 result for $C_{96}H_{24}$. This disagreement is greater than the percentage difference between the MP2 and PBE0 values of the in-plane dipole polarizability and could reflect differences in these two theoretical methods for describing the molecular quadrupole polarizabilities.

3.3. Model Validation: Electrostatics and Repulsion

Having verified that the polarization model yields accurate polarizabilities and a reasonable polarization potential, we turn our attention to short-range repulsion and electrostatics. To assess the quality of the one-electron model when repulsion and electrostatics are included, comparisons are made to results at the KT level as well as EA-EOM-CCSD and EA-EOM-MP2 calculations on coronene with enhanced nuclear charges. Figure 7 plots the model Hamiltonian, KT, and EA-EOM values of the EBE as a function of the excess molecular charge.

As noted in section 2.3, the scaling of atomic charges of coronene introduces a long-range Coulomb potential, which binds Rydberg states so long as sufficiently flexible basis sets are used. In the absence of correlation effects in the ab initio calculations (KT) and the one-electron model without polarization, $V_{rep,es}$, the bound states are necessarily Rydberg in nature. However, it is not obvious a priori whether the lowest energy state bound in EA-EOM or the one-electron model including polarization, $V_{pol,rep,es}$, will be Rydberg, NVCB, or a strongly mixed state. Regardless of the nature of this state, this provides additional data points for assessing the performance of the model when polarization effects are included.

We consider first the binding energies in the absence of correlation/polarization effects. The ab initio KT EBEs and the corresponding model potential results, $V_{rep,es}$, are in excellent agreement This validates the description of the electrostatics and the short-range repulsion in the model. In addition, these EBEs show a quadratic dependence on Z_{ex}, consistent with the ground state being Rydberg in nature [86]. On the other hand, the EBEs calculated using the EA-EOM methods or the full model potential, $V_{pol,rep,es}$, display a near linear dependence on Z_{ex} indicating that these correspond to non-valence anions (stabilized by the addition of the Coulomb potential) rather than Rydberg states. Again, for testing the performance of the model, which of these interpretations is more correct is not particularly relevant.

Note that for charge-enhanced coronene, the model with polarization ($V_{pol,rep,es}$), underestimates the EA-EOM EBEs by as much as 20%. Factors contributing to this include the fact that the model underestimates the PBE0 in-plane polarizability by $\sim 6\%$ and also that the use of a 2 bohr spacing of the DVR grid introduces errors of $\sim 5.6\%$ on average in the binding energy of the NVCB anion of coronene with enhanced nuclear charge. We do not find this particularly concerning because we are targeting the NVCB anions of the larger charge-neutral PAHs where the error of the model polarizabilities with respect PBE0 and MP2 are smaller. The agreement between the KT and model $V_{rep,es}$ EBEs demonstrates what we had hoped to find with this data set, namely the

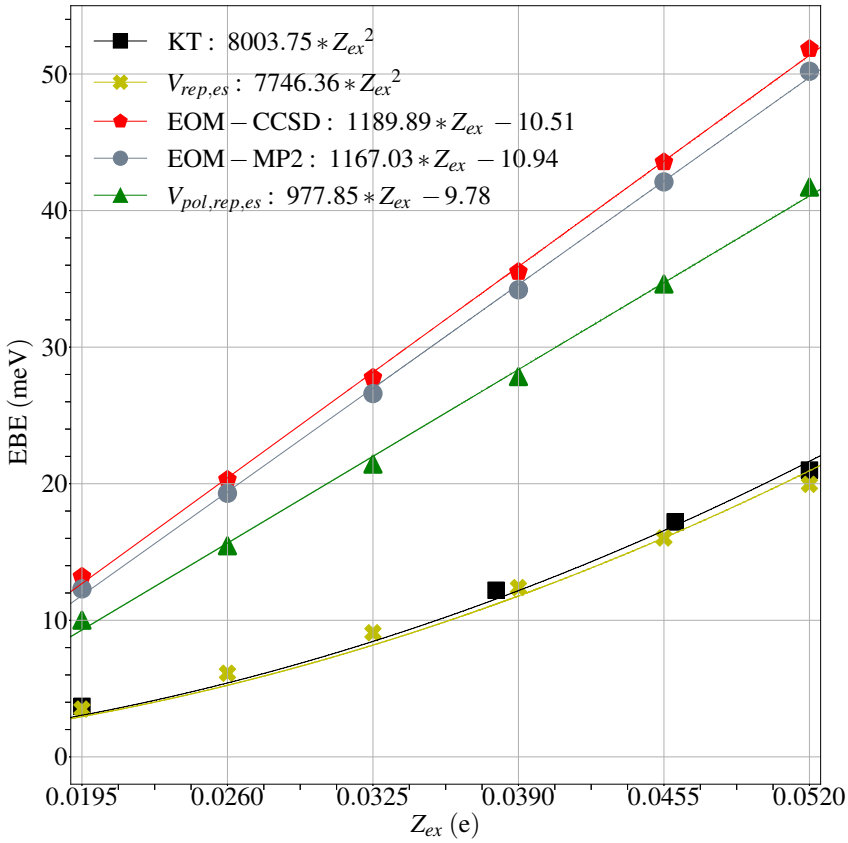

Figure 7: Plot of the electron binding energy (EBE) of the lowest energy NVCB state of charge stabilized coronene against excess molecular charge (Z_{ex}). Note that a positive EBE indicates that the anion is bound. The plot includes the EBE obtained via EA-EOM-CCSD, EA-EOM-MP2, Koopmans' Theorem (KT), and the model Hamiltonian. The EBEs of EA-EOM-CCSD, EA-EOM-MP2, and model Hamiltonian with polarization, $V_{pol,rep,es}$, are fit by linear functions of Z_{ex}, while the KT and model Hamiltonian without polarization $V_{rep,es}$ results are fit to curves proportional to Z_{ex}^2. The legend of the figure shows the fit coefficients for each data set. Image generated using Matplotlib [82].

model electrostatics and repulsion is performing well.

3.4. Binding Energies of Charge-Neutral PAH NVCB Anions

Next, we report the EBEs of the ground state NVCB anion of PAHs $C_{54}H_{18}$ to $C_{294}H_{42}$. Table 3 reports the EBEs for V_{pol} as well as the $V_{pol,rep}$ and $V_{pol,rep,es}$ combinations of the model potential components.

As can be seen from the results reported in table 3, polarization and repulsion are the largest contributions in magnitude to the total binding energy, with the repulsive potential greatly reducing the EBEs obtained using the polarization component alone. Electrostatics are less important relative to the contributions of polarization and repulsion to the EBEs, but do lead to non-negligible reductions of the EBEs of the three

Table 3: Electron binding energy in meV for the lowest energy NVCB state for PAHs $C_{6n^2}H_{6n}$ (n = 3−7) for the model Hamiltonian with polarization alone (V_{pol}), with both polarization and repulsion ($V_{pol,rep}$), and the full potential including electrostatic charges through quadrupoles on all atoms ($V_{pol,rep,es}$).

PAH	V_{pol}	$V_{pol,rep}$	$V_{pol,rep,es}$
$C_{54}H_{18}$	2042.9	12.2	12.3
$C_{96}H_{24}$	2370.3	55.8	49.2
$C_{150}H_{30}$	2581.1	113.8	93.8
$C_{216}H_{36}$	2727.8	173.1	139.1
$C_{294}H_{42}$	2835.6	227.1	182.8

larger PAHs, with the largest reduction being ∼ 20%. The EBE of $C_{54}H_{18}$ when using the full model potential ($V_{pol,rep,es}$) is 12.3 meV, which is in good agreement with Voora and Jordan's EA-EOM-MP2 result of 12.6 meV [29].

3.5. Understanding Edge Localization: Potential Slices and Density Differences

As noted in the previous section, the model closely reproduces the EA-EOM-MP2 binding energy for $C_{54}H_{18}$. However, this is not surprising as the parameters in the repulsive potential were chosen so as to give this outcome. We have also shown that this choice of the repulsive parameters performs reasonably well for the charge enhanced $C_{24}H_{12}$ species. We note also that for other systems (e.g., water clusters) it has been established the values of the repulsive parameters determined on one size cluster, gives quantitatively accurate EBEs when applied to a wide range of other water clusters (for which EOM calculations are possible to check the performance of the model [17, 22].

Having established the above points, there are two questions that have yet to be addressed. Is the edge localization reported by Voora and Jordan for the ground state NVCB anion of $C_{54}H_{18}$ purely an electrostatic effect, and does this behavior persist for appreciably larger PAHs? To answer these questions, we plot for $C_{54}H_{18}$ and $C_{294}H_{42}$ one-dimensional slices along the x axis for the interaction between the excess electron (modeled via a negative point charge) with the following potential components: V_{pol}, V_{rep}, and V_{es}, as well as the combinations $V_{pol,rep}$, and $V_{pol,rep,es}$. Slices are taken at four values of z above the plane of the ring systems to illustrate how the interaction changes with vertical separation of the excess electron from the PAHs. Figures 8a–8h show the results.

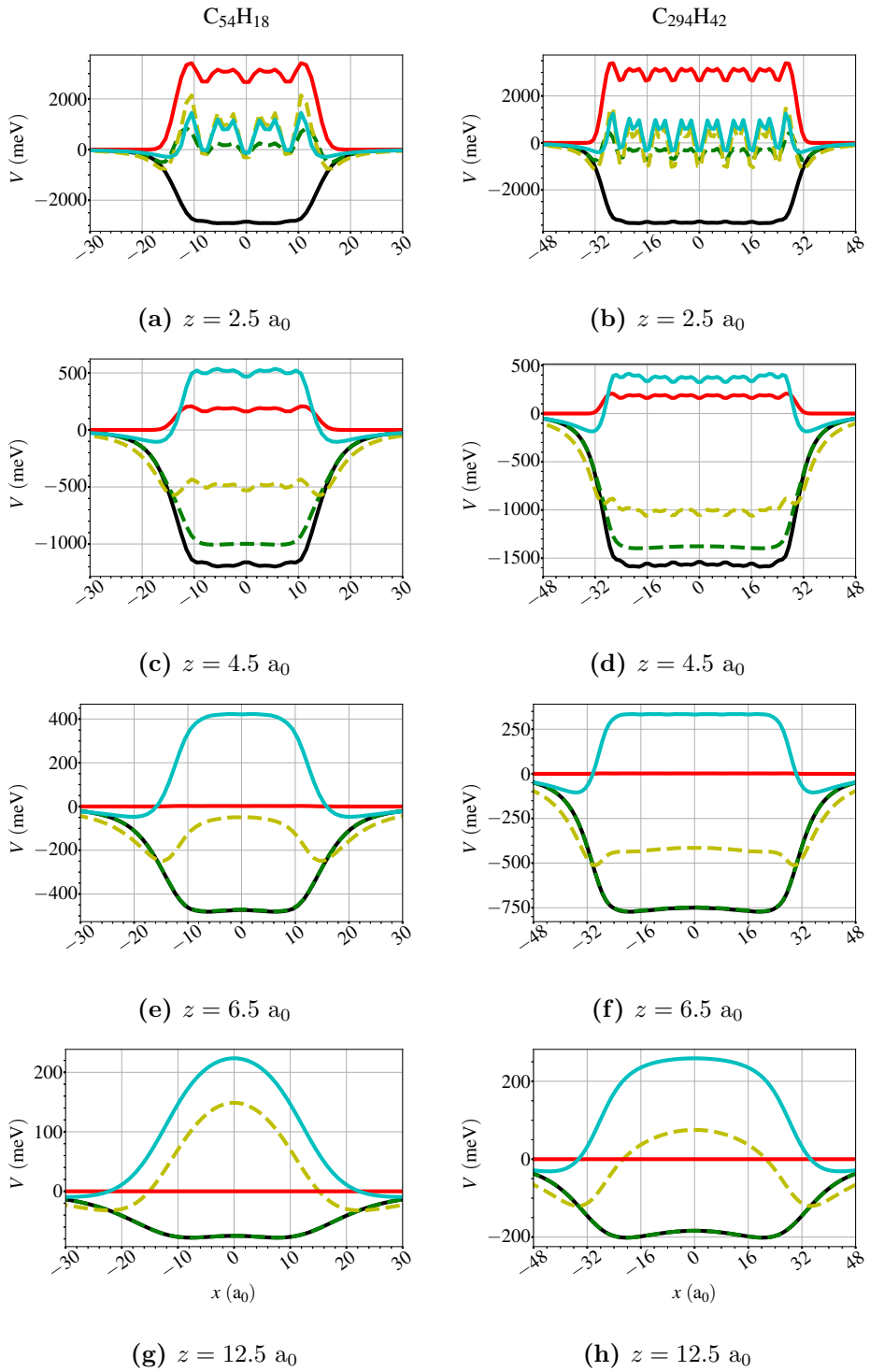

(a) $z = 2.5$ a$_0$ **(b)** $z = 2.5$ a$_0$

(c) $z = 4.5$ a$_0$ **(d)** $z = 4.5$ a$_0$

(e) $z = 6.5$ a$_0$ **(f)** $z = 6.5$ a$_0$

(g) $z = 12.5$ a$_0$ **(h)** $z = 12.5$ a$_0$

Figure 8: One-dimensional slices of the model potential for a negative point charge (e^-) interacting with $C_{54}H_{18}$ (a,c,e,g) and $C_{294}H_{42}$ (b,d,f,h). All images represent a slice along x axis. The distance of the slice above the plane of atoms (z) is fixed at the value indicated by the text at the bottom of each plot. Each set of images shows the potential due to polarization alone (━ V_{pol}), repulsion (━ V_{rep}), electrostatics (━ V_{es}), both polarization and repulsion (▬ $V_{pol,rep}$), and the full model potential employing electrostatic charges through quadrupoles on all atoms (▬ $V_{pol,rep,es}$). Images generated using Matplotlib [82].

Inspecting the slices of the individual potential components for $C_{54}H_{18}$ and $C_{294}H_{42}$ one sees that the electrostatic potentials (V_{es}) are primarily repulsive above the plane of the atoms, i.e. $-11 < x < 11$ and $-24 < x < 24$ a_0 for $C_{54}H_{18}$ and $C_{294}H_{42}$ respectively. At the shortest distance considered, $z = 2.5$ a_0, both the repulsive potentials (V_{rep}) and V_{es} display oscillations as one scans across the surface. Although, V_{es} oscillates between negative and positive values at $z = 2.5$ a_0, the average electrostatic potential is repulsive in this region. These fluctuations weaken for vertical separations of $z > 2.5$ a_0 due to its short-range nature. By $z = 6.5$ a_0, the effects of V_{rep} are negligible making V_{es} and V_{pol} the dominate contributions, which is to be expected. A key finding is that V_{es} is repulsive above and below the plane of the molecules, but it is attractive outside the plane of atoms, $|x| > 11$ and $|x| > 24$ a_0 for $C_{54}H_{18}$ and $C_{294}H_{42}$ respectively, with the deepest point in V_{es} appearing in this region for each value of z considered. The behavior of the electrostatic potential makes non-negligible modifications to the shape of full model potential $V_{pol,rep,es}$, that lowers the probability of the excess electron occupying space above and below the plane of atoms and increases the probability of the electron localizing near the C-H bonds. These observations indicate that the edge localization observed by Voora and Jordan is an electrostatic effect as they had conjectured.

One attribute distinguishing the electrostatic potentials of $C_{54}H_{18}$ and $C_{294}H_{42}$ is the magnitude of V_{es}. For $z \geq 4.5$ a_0, the electrostatic interaction above the plane of atoms is less repulsive for $C_{294}H_{42}$ than $C_{54}H_{18}$. At $z = 4.5$ a_0, the electrostatics and repulsion above $C_{294}H_{42}$ is weak enough relative to polarization that $V_{pol,rep,es}$ is more attractive at the center than at the edges of the PAH. This can be attributed to, in part, the vanishing of atomic charges and dipoles on the central carbon atoms with increasing system size, as the impact of the edge C-H bonds on the atomic electrostatic moments is smallest at the center of these PAHs.

The potential slices in figures 8a–8h demonstrate that the electrostatic potential is repulsive above and below the π system and introduces attractive potential wells along the edges. To clearly illustrate the impact of electrostatics on the electronic density we plot the change in electronic density of the lowest energy NVCB state of the PAHs when electrostatics are introduced into the model Hamiltonian, i.e. $\Delta\rho(V_{es}) = \rho(V_{pol,rep,es}) - \rho(V_{pol,rep})$. Figure 9 depicts the density differences for PAHs $C_{6n^2}H_{6n}$ $(n = 3 - 7)$.

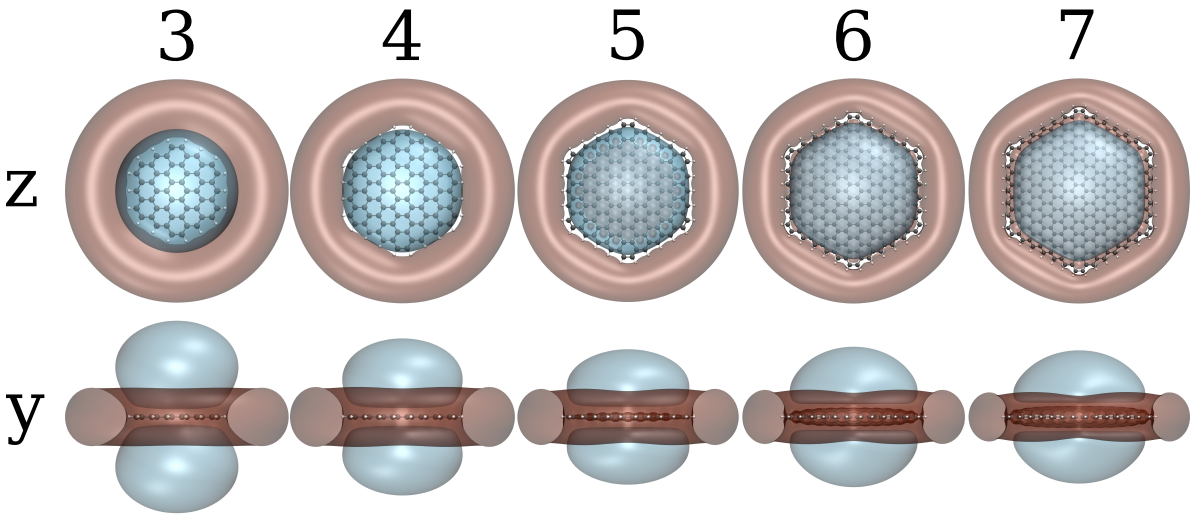

Figure 9: Change in electronic density due to electrostatics for the lowest energy NVCB anion of PAHs $C_{6n^2}H_{6n}$ (n = 3−7). The results were obtained by calculating the electronic density of the NVCB anion while employing the full model potential $V_{pol,rep,es}$ and subtracting the density obtained in the absence of electrostatics $V_{pol,rep}$, i.e. $\Delta\rho(V_{es}) = \rho(V_{pol,rep,es}) - \rho(V_{pol,rep})$. Each column reports results for a different PAH as indicated by the number at the top of the image (e.g. $C_{6n^2}H_{6n}$ (n = 3) is $C_{54}H_{18}$). Two perspectives of the same plot are shown for each PAH with labels of, "z," or, "y". The top row of density difference plots denoted as, "z," in the figure are oriented along the C_6 rotational axis and the bottom row of plots denoted as, "y," in the figure are oriented along one of the C_2 rotational axis. The surfaces are drawn at an isovalue such that they enclose 90% of the change in the excess electron's charge density. Voids in the density difference appearing as white space are portions that would be captured at smaller isovalues. Blue coloration indicates a decrease in electronic density and red coloration indicates an increase in electronic density. Images generated using VMD [67].

For all PAHs considered the region of space above and below the π system experience a decrease in electron density, whereas there is a buildup of electron density around the perimeter of the PAHs upon the inclusion of electrostatics. This illustrates that the electrostatics make non-trivial changes to the charge distribution of the NVCB states of PAHs and that the edge localization of the single particle orbitals is a consequence of electrostatics, just as Voora and Jordan had conjectured. Furthermore, the density differences show that preferential binding at the edges persists for larger PAHs, which consistent with the behavior of $V_{pol,rep,es}$ observed in figures 8a–8f.

4. Conclusions

This work presents progress towards a one-electron model in the code PISCES, aimed at treating NVCB anions of large hexagonal PAHs with molecular formula $C_{6n^2}H_{6n}$ where $n = 3, 4, 5, \ldots$ The results provide insight into the nature of the NVCB anions of these molecules, which would be inaccessible to high accuracy ab initio QM methods such as EA-EOM-CCSD. The one-electron model Hamiltonian employed in this work allows us to inspect the contributions of polarization, repulsion, and electrostatics to the NVCB

anions. In doing so, we assessed the impact of electrostatics on the electron binding energy and charge distribution of the orbital associated with the excess electron.

Good agreement was observed between the dipole polarizabilities of the model and those from PBE0 and MP2 calculations. Charge flow polarization is found to dominate the model in-plane polarizability components ($\alpha_{xx/yy}$) of PAH systems above $C_{54}H_{18}$. We compared scans of the polarization potential obtained from model calculations against results from MP2 and PBE0 calculations. Modest discrepancies were observed relative to MP2 and PBE0. These discrepancies tend to decrease at larger separations between the point charge and PAHs. The model underestimates the magnitude of the polarization potential when a point charge is perpendicular to the plane of atoms. It is our current belief that this is the result of higher order polarizabilities not explicitly accounted for in the model, which we plan to explore in future work.

It was shown that inclusion of electrostatics reduces the binding energy of the ground state NVCB anions of the larger hexagonal PAHs studied by up to 20%. In addition, the inclusion of electrostatics shifts the charge density of the excess electron toward the periphery of the ring systems. Future work includes a more rigorous parameterization of the repulsive Gaussians using reference EOM calculations on the ground and first electronically excited NVCB anions of larger PAHs.

References

[1] Simons J and Jordan K D 1987 *Chem. Rev.* **87**(3) 535–555

[2] Simons J 2008 *J. Phys. Chem. A* **112**(29) 6401–6511

[3] Sommerfeld T 2013 *J. Chem. Theory Comput.* **9**(11) 4866–4873

[4] Janesko B G, Scalmani G and Frisch M J 2015 *Phys. Chem. Chem. Phys.* **17**(28) 18305–18317

[5] Verlet J R R, Anstöter C S, Bull J N and Rogers J P 2020 *J. Phys. Chem. A* **124**(18) 3507–3519

[6] Rogers J P, Anstöter C S and Verlet J R R 2018 *Nat. Chem.* **10**(3) 341–346

[7] Bull J N, Anstöter C S and Verlet J R R 2019 *Nat. Chem.* **10**(1) 5820

[8] Sommerfeld T 2004 *J. Chem. Phys.* **121**(9) 4097–4104

[9] Hao H, Shee J, Upadhyay S, Ataca C, Jordan K D and Rubenstein B M 2018 *J. Phys. Chem. Lett.* **9**(21) 6185–6190

[10] Voora V K, Kairalapova A, Sommerfeld T and Jordan K D 2017 *J. Chem. Phys.* **147**(21) 214114

[11] Herbert J M 2015 The quantum chemistry of loosely-bound electrons *(Reviews in Computational Chemistry* vol 28) ed Abby L Parrill K B L (Hoboken, NJ: John Wiley & Sons, Ltd) chap 8, pp 391–517

[12] Voora V K, Cederbaum L S and Jordan K D 2013 *J. Phys. Chem. Lett.* **4**(6) 849–853

[13] Voora V K and Jordan K D 2014 *Nano Lett.* **14**(8) 4602–4606

[14] Choi T H and Jordan K D 2019 *Faraday Discuss.* **217**(0) 547–560

[15] Choi T H, Vazhappilly T and Jordan K D 2017 *J. Chem. Phys.* **147**(16) 161717

[16] Upadhyay S, Dumi A, Shee J and Jordan K D 2020 *J. Chem. Phys.* **153**(22) 224118

[17] Voora V K, Ding J, Sommerfeld T and Jordan K D 2013 *J. Phys. Chem. B* **117**(16) 4365–4370

[18] Wallqvist A, Thirumalai D and Berne B J 1986 *J. Chem. Phys.* **85** 1583–1591

[19] Wallqvist A, Thirumalai D and Berne B J 1987 *J. Chem. Phys.* **86** 6404–6418

[20] Barnett R N, Landman U, Cleveland C L and Jortner J 1988 *J. Chem. Phys.* **88** 4421–4428

[21] Jacobson L D, Williams C F and Herbert J M 2009 *J. Chem. Phys.* **130** 124115

[22] Wang F and Jordan K D 2002 *J. Chem. Phys.* **116** 6973–6981

[23] Sommerfeld T, Bhattarai B, Vysotskiy V P and Cederbaum L S 2010 *J. Chem. Phys.* **133**(11) 114301

[24] Bezchastnov V G, Vysotskiy V P and Cederbaum L S 2011 *Phys. Rev. Lett.* **107**(13) 133401

[25] Voora V K and Jordan K D 2014 *J. Phys. Chem. A* **118**(35) 7201–7205

[26] Field D, Jones N C and Ziesel J P 2004 *Phys. Rev. A* **69**(5) 052716

[27] Rogers J P, Anstöter C S and Verlet J R R 2018 *J. Phys. Chem. Lett.* **9**(10) 2504–2509

[28] Dougherty D B, Feng M, Petek H, Yates J T and Zhao J 2012 *Phys. Rev. Lett.* **109**(26) 266802

[29] Voora V K and Jordan K D 2015 *J. Phys. Chem. Lett.* **6**(20) 3994–3997

[30] Fock V 1930 *Zeitschrift für Physik* **61**(1) 126–148

[31] Roothaan C C J 1951 *Rev. Mod. Phys.* **23**(2) 69

[32] Hartree D R 1928 *Math. Proc. Cambridge* **24**(1) 89–110

[33] Møller C and Plesset M S 1934 *Phys. Rev.* **46**(7) 618–622

[34] Raghavachari K, Trucks G W, Pople J A and Head-Gordon M 1989 *Chem. Phys. Lett.* **157**(6) 479–483

[35] Berland K, Cooper V R, Lee K, Schröder E, Thonhauser T, Hyldgaard P and Lundqvist B I 2015 *Rep. Prog. Phys.* **78**(6) 066501

[36] Hamada I 2014 *Phys. Rev. B* **89**(12) 121103

[37] Hamada I, Hamamoto Y and Morikawa Y 2017 *J. Chem. Phys.* **147**(4) 044708

[38] Nooijen M and Bartlett R J 1995 *J. Chem. Phys.* **102**(9) 3629–3647

[39] Nooijen M and Snijders J G 1995 *J. Chem. Phys.* **102**(4) 1681–1688

[40] Stanton J F and Gauss J 1995 *J. Chem. Phys.* **103**(3) 1064–1076

[41] Dutta A K, Saitow M, Riplinger C, Neese F and Izsák R 2018 *J. Chem. Phys.* **148**(24) 244101

[42] Dutta A K, Saitow M, Demoulin B, Neese F and Izsák R 2019 *J. Chem. Phys.* **150**(16) 164123

[43] Sommerfeld T, DeFusco A and Jordan K D 2008 *J. Phys. Chem. A* **112**(44) 11021–11035

[44] Turi L and Rossky P J 2012 *Chem. Rev.* **112**(11) 5641–5674

[45] Sommerfeld T, Choi T H, Voora V K and Jordan K D Pittsburgh InfraStructure for Clusters with Excess ElectronS, (PISCES) www.pisces.pitt.edu

[46] Kocman M, Pykal M and Jurečka P 2014 *Phys. Chem. Chem. Phys.* **16**(7) 3144–3152

[47] Zhu S, Wang L, Li B, Song Y, Zhao X, Zhang G, Zhang S, Lu S, Zhang J, Wang H, Sun H and Yang B 2014 *Carbon* **77** 462–472

[48] Tian P, Tang L, Teng K and Lau S 2018 *Materials Today Chemistry* **10** 221–258

[49] N'Diaye A T, Engler M, Busse C, Wall D, Buckanie N, Meyer zu Heringdorf F J, van Gastel R, Poelsema B and Michely T 2009 *New J. Phys.* **11** 023006

[50] Mayer A and Åstrand P O 2008 *J. Phys. Chem. A* **112**(6) 1277–1285

[51] Mayer A 2007 *Phys. Rev. B* **75**(4) 045407

[52] Rappé A K and Goddard W A 1991 *J. Phys. Chem.* **95**(8) 3358–3363

[53] Poier P P and Jensen F 2019 *J. Chem. Theory Comput.* **15**(5) 3093–3107

[54] Chen J and Martínez T J 2007 *Chem. Phys. Lett.* **438**(4) 315–320

[55] Lee Warren G, Davis J E and Patel S 2008 *J. Chem. Phys.* **128**(14) 144110

[56] Champagne B, Perpète E A, van Gisbergen S J A, Baerends E J, Snijders J G, Soubra-Ghaoui C, Robins K A and Kirtman B 1998 *J. Chem. Phys.* **109**(23) 10489–10498

[57] Kirtman B, Lacivita V, Dovesi R and Reis H 2011 *J. Chem. Phys.* **135**(15) 154101

[58] Yanai T, Tew D P and Handy N C 2004 *Chem. Phys. Lett.* **393**(1) 51–57

[59] Adamo C and Barone V 1999 *J. Chem. Phys.* **110**(13) 6158–6170

[60] Zhu Y, Murali S, Cai W, Li X, Suk J W, Potts J R and Ruoff R S 2010 *Adv. Mater.* **22**(35) 3906–3924

[61] Parrish R M, Burns L A, Smith D G, Simmonett A C, DePrince A E, Hohenstein E G, Bozkaya U, Sokolov A Y, Di Remigio R, Richard R M, Gonthier J F, James A M, McAlexander H R, Kumar A, Saitow M, Wang X, Pritchard B P, Verma P, Schaefer H F, Patkowski K, King R A, Valeev E F, Evangelista F A, Turney J M, Crawford T D and Sherrill C D 2017 *J. Chem. Theory Comput.* **13**(7) 3185–3197

[62] Turney J M, Simmonett A C, Parrish R M, Hohenstein E G, Evangelista F A, Fermann J T, Mintz B J, Burns L A, Wilke J J, Abrams M L, Russ N J, Leininger M L, Janssen C L, Seidl E T, Allen W D, Schaefer H F, King R A, Valeev E F, Sherrill C D and Crawford T D 2012 *WIREs Comput Mol Sci* **2**(4) 556–565

[63] Smith D G A, Burns L A, Simmonett A C, Parrish R M, Schieber M C, Galvelis R, Kraus P, Kruse H, Di Remigio R, Alenaizan A, James A M, Lehtola S, Misiewicz J P, Scheurer M, Shaw R A, Schriber J B, Xie Y, Glick Z L, Sirianni D A, O'Brien J S, Waldrop J M, Kumar A, Hohenstein E G, Pritchard B P, Brooks B R, Schaefer H F, Sokolov A Y, Patkowski K, DePrince A E, Bozkaya U, King R A, Evangelista F A, Turney J M, Crawford T D and Sherrill C D 2020 *J. Chem. Phys.* **152**(18) 184108

[64] Rappoport D and Furche F 2010 *J. Chem. Phys.* **133**(13) 134105

[65] Weigend F 2008 *J. Comput. Chem.* **29**(2) 167–175

[66] Hellweg A and Rappoport D 2015 *Phys. Chem. Chem. Phys.* **17**(2) 1010–1017

[67] Humphrey W, Dalke A and Schulten K 1996 *J. Mol. Graphics* **14**(1) 33–38

[68] Virtanen P, Gommers R, Oliphant T E, Haberland M, Reddy T, Cournapeau D, Burovski E, Peterson P, Weckesser W, Bright J, van der Walt S J, Brett M, Wilson J, Millman K J, Mayorov N, Nelson A R J, Jones E, Kern R, Larson E, Carey C J, Polat İ, Feng Y, Moore E W, VanderPlas J, Laxalde D, Perktold J, Cimrman R, Henriksen I, Quintero E A, Harris C R, Archibald A M, Ribeiro A H, Pedregosa F, van Mulbregt P and SciPy 10 Contributors 2020 *Nature Methods* **17** 261–272

[69] Hirshfeld F L 1977 *Theor. Chim. Acta* **44**(2) 129–138

[70] Frisch M J, Trucks G W, Schlegel H B, Scuseria G E, Robb M A, Cheeseman J R, Scalmani G, Barone V, Petersson G A, Nakatsuji H, Li X, Caricato M, Marenich A V, Bloino J, Janesko B G, Gomperts R, Mennucci B, Hratchian H P, Ortiz J V, Izmaylov A F, Sonnenberg J L, Williams-Young D, Ding F, Lipparini F, Egidi F, Goings J, Peng B, Petrone A, Henderson T, Ranasinghe D, Zakrzewski V G, Gao J, Rega N, Zheng G, Liang W, Hada M, Ehara M, Toyota K, Fukuda R, Hasegawa J, Ishida M, Nakajima T, Honda Y, Kitao O, Nakai H, Vreven T, Throssell K, Montgomery Jr J A, Peralta J E, Ogliaro F, Bearpark M J, Heyd J J, Brothers E N, Kudin K N, Staroverov V N, Keith T A, Kobayashi R, Normand J, Raghavachari K, Rendell A P, Burant J C, Iyengar S S, Tomasi J, Cossi M, Millam J M, Klene M, Adamo C, Cammi R, Ochterski J W, Martin R L, Morokuma K, Farkas O, Foresman J B and Fox D J 2016 Gaussian 16 Revision A.03 gaussian Inc. Wallingford CT

[71] Nestmann B and Peyerimhoff S D 1985 *J. Phys. B: At. Mol. Phys.* **18**(4) 615

[72] Nestmann B M and Peyerimhoff S D 1985 *J. Phys. B: At. Mol. Phys.* **18**(21) 4309

[73] Sangwan P and Vikas 2016 *J. Chem. Phys.* **144**(4) 044305

[74] Whitehead A, Barrios R and Simons J 2002 *J. Chem. Phys.* **116**(7) 2848–2851

[75] Widmark P O, Malmqvist P Å and Roos B O 1990 *Theoretica chimica acta* **77**(5) 291–306

[76] Stanton J F, Gauss J, Cheng L, Harding M E, Matthews D A and Szalay P G CFOUR, Coupled-Cluster techniques for Computational Chemistry, a quantum-chemical program package With contributions from A.A. Auer, R.J. Bartlett, U.

Benedikt, C. Berger, D.E. Bernholdt, Y.J. Bomble, O. Christiansen, F. Engel, R. Faber, M. Heckert, O. Heun, M. Hilgenberg, C. Huber, T.-C. Jagau, D. Jonsson, J. Jusélius, T. Kirsch, K. Klein, W.J. Lauderdale, F. Lipparini, T. Metzroth, L.A. Mück, D.P. O'Neill, D.R. Price, E. Prochnow, C. Puzzarini, K. Ruud, F. Schiffmann, W. Schwalbach, C. Simmons, S. Stopkowicz, A. Tajti, J. Vázquez, F. Wang, J.D. Watts and the integral packages MOLECULE (J. Almlöf and P.R. Taylor), PROPS (P.R. Taylor), ABACUS (T. Helgaker, H.J. Aa. Jensen, P. Jorgensen, and J. Olsen), and ECP routines by A. V. Mitin and C. van Wüllen. For the current version, see `http://www.cfour.de`.

[77] Koopmans T 1934 *Physica* **1**(1) 104–113

[78] Brzeski J and Jordan K D 2021 University of Pittsburgh, Pittsburgh, PA. Unpublished data

[79] Stone A J 2005 *J. Chem. Theory Comput.* **1**(6) 1128–1132

[80] Dunning T H 1989 *J. Chem. Phys.* **90**(2) 1007–1023

[81] Lu T and Chen F 2012 *Journal of Computational Chemistry* **33** 580–592

[82] Hunter J D 2007 *Comput. Sci. Eng.* **9**(3) 90–95

[83] Smith S M, Markevitch A N, Romanov D A, Li X, Levis R J and Schlegel H B 2004 *J. Phys. Chem. A* **108**(50) 11063–11072

[84] Champagne B, Mosley D H and André J M 1994 *J. Chem. Phys.* **100**(3) 2034–2043

[85] Binkley J S, Pople J A and Hehre W J 1980 *Journal of the American Chemical Society* **102** 939–947

[86] Simons J 2021 *J. Phys. Chem. A* **125** 7735–7749